

Two-Tier Compatibility of Superelastic Bicrystal Micropillar at Grain Boundary

Mostafa Karami, Zeyuan Zhu, Zhuohui Zeng, Nobumichi Tamura, Yong Yang, and Xian Chen*

Cite This: <https://dx.doi.org/10.1021/acs.nanolett.0c03486>

Read Online

ACCESS |

Metrics & More

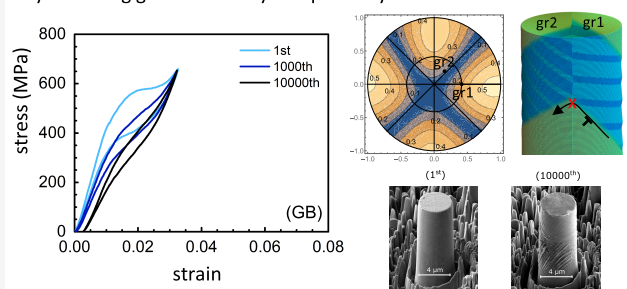
Article Recommendations

Supporting Information

ABSTRACT: Both crystallographic compatibility and grain engineering are super critical to the functionality of shape memory alloys, especially at micro- and nanoscales. Here, we report a bicrystal $\text{CuAl}_{24}\text{Mn}_9$ micropillar engraved at a high-angle grain boundary (GB) that exhibits enhanced reversibility under very demanding driving stress (about 600 MPa) over 10 000 transformation cycles despite its lattice parameters are far from satisfying any crystallographic compatibility conditions. We propose a new compatibility criterion regarding the GB for textured shape memory alloys, which suggests that the formation of GB compatible twin laminates in neighboring textured grains activates an interlock mechanism, which prevents dislocations from slipping across GB.

KEYWORDS: Nanomechanics, Micropillar compression, Grain Boundary, Compatibility

Enhanced transformability and suppressed slip of CuAlMn micropillar by achieving grain boundary compatibility



The magnificent self-expanding and mechanical damping features of shape memory alloys (SMAs) make them the primary metals for biomedical and microelectronic applications.^{1–6} In tandem with the rapid growth of nanofabrication technologies,^{7,8} more complicated functional devices can be made at smaller scales, which promotes the development of shape memory alloys for the tiny neural stents for brains.^{9,10} These small and precise micro- and nanodevices demand a more reliable superelastic response upon numerous superelastic cycles.

A well-accepted theory that intrinsically improves the transformability and lowers the functional fatigue is to make the material satisfy the compatibility conditions.¹¹ These conditions are the geometric measures of lattice mismatch for symmetry-breaking structural transformation through a coherent transformation stretch tensor.¹² Such a stretch tensor depends only on the lattice parameters of parent and product phases and can be determined algorithmically.¹³ The satisfaction of all compatibility conditions by special lattice parameters guarantees a stress-free interface configuration between the parent and product phases. In this scenario, the bulk elastic energy dissipation is minimized during the phase transformation; as a result, the material shows low hysteresis and high reversibility. Experimentally, the lattice parameters can be systematically tuned to fulfill the compatibility conditions by slight chemical doping, which underlies a design strategy for alloy development. Guided by this design strategy, people have successfully demonstrated the lowered thermal-hysteresis and the improved functional fatigue life in both NiTi- and Cu-based shape memory alloys.^{14–16} At small scales, some very special

alloys can reach millions of nondegradable superelastic cycles in thin-films¹⁷ and micropillars.¹⁸ Similar experimental evidence are also reported in phase transforming ceramics at small scales.^{19,20}

Engineering grain morphology is an alternative way to improve the fatigue life for SMAs independent of tuning lattice parameters. Through the repeated cold rolling processes, the grains can be reduced to nanometer scales constrained by numerous nontransforming grain boundaries. This has been successfully demonstrated in Nitinol, that is, binary $\text{Ni}_{50}\text{Ti}_{50}$ alloy.²¹ Although the B2 (cubic) to B19' (monoclinic) phase transformation of NiTi is very incompatible²² without additional chemical doping, the engineered NiTi micropillar with ultrafine grains exhibits prominent superelasticity even after 1 million demanding stress-induced transformation cycles.^{23,24} It strongly suggests that the grain boundaries are crucial to the functional fatigue of the superelastic alloy. In nanocrystalline superelastic micropillar, it was conjectured that the grain boundary can mediate the discontinuities between neighboring grains, thus suppressing the fatigue caused by plastic deformations and microcrack propagation.²¹ This grain boundary mediated mechanism implies another level of compatibility, however the

Received: August 28, 2020

Revised: October 8, 2020

quantitative measures for such a mediation are not thoroughly rationalized. So far, there has not been much experimental work directly characterizing the mechanical properties of a single grain boundary with textures.

Can the phase transformation of a shape memory polycrystal be still highly reversible without fulfilling the compatibility conditions by lattice parameters? What role does the grain boundary (GB) play in a textured polycrystal under stress-induced phase transformation? In this paper, we study these emerging problems using a phase-transforming bicrystal micropillar with a single GB under the nanomechanical experiments. The studied alloy is $\text{CuAl}_{24}\text{Mn}_9$, whose lattice parameters are far from satisfying any intrinsic compatibility conditions. This alloy family suffers greatly from the functional degradation problems, especially for those polycrystalline alloys under the cyclic stress-induced transformations.^{25,26} Similar to its sibling ternary and quaternary alloys,^{26–28} the single crystal $\text{CuAl}_{24}\text{Mn}_9$ micropillars show anisotropic superelastic strains corresponding to different critical driving stresses.

Unlike the common Cu-based shape memory alloys undergoing cubic to monoclinic transformation, the chosen $\text{CuAl}_{24}\text{Mn}_9$ alloy transforms between cubic austenite and orthorhombic martensite. The martensite crystal structure was carefully characterized by synchrotron X-ray microdiffraction at the Advanced Light Source Beamline 12.3.2, Lawrence Berkeley National Lab. The symmetry of martensite is determined to be $Pmmm$ by the newly established crystallographic theory of derived crystal structure.²⁹ Using a monochromator energy scan,³⁰ we collected more than 20 peaks diffracted by distinct crystallographic planes from which we obtained the refined lattice parameters for the orthorhombic martensite as $a = 4.43196 \text{ \AA}$, $b = 5.34533 \text{ \AA}$, $c = 4.26307 \text{ \AA}$. The symmetry of austenite phase is confirmed to be $Fm\bar{3}m$ by synchrotron X-ray Laue microdiffraction with the refined lattice parameter $a_0 = 5.87897 \text{ \AA}$. On the basis of the lattice parameters, we used the StrucTrans algorithm¹³ to calculate the transformation stretch tensor

$$\mathbf{U} = \frac{1}{\sqrt{2}a_0} \begin{bmatrix} a+c & a-c & 0 \\ a-c & a+c & 0 \\ 0 & 0 & \sqrt{2}b \end{bmatrix} \quad (1)$$

with ordered eigenvalues $(\lambda_1, \lambda_2, \lambda_3) = \left(\frac{b}{a_0}, \frac{\sqrt{2}c}{a_0}, \frac{\sqrt{2}a}{a_0}\right)$ in which $\lambda_2 = 1.0255$. According to crystallographic compatibility theory,^{11,12} the closeness of λ_2 to 1 strongly affects the reversibility of the phase transformation for shape memory alloys.^{11,14,16–18} This material is far from satisfying the compatibility condition compared to other Cu-based SMAs shown in Table 1. To minimize the lattice mismatch across the austenite/martensite interface, the alloy has to form twin laminates that are finely branched to austenite through an elastic

Table 1. Comparison of the Primary Compatibility Condition $\lambda_2 = 1$ in Cu-Based Shape Memory Alloys

SMAs	phase transformation	$ \lambda_2 - 1 $
$\text{CuAl}_{14}\text{Ni}_4$ ³¹	cubic to monoclinic	0.00341
$\text{CuZn}_{15}\text{Al}_{17}$ ³²	cubic to monoclinic	0.01264
$\text{CuAu}_{30}\text{Zn}_{45}$ ¹⁶	cubic to monoclinic	0.00061
$\text{CuAl}_{17}\text{Mn}_{10}$ ²⁷	cubic to monoclinic	0.02587
$\text{CuAl}_{24}\text{Mn}_9$ (this work)	cubic to orthorhombic	0.02550

transition layer in which the nontransforming defects would nucleate and propagate, thus the functionality of the material degrades over transformation cycles.

A very large thermal hysteresis of $38 \text{ }^\circ\text{C}$ is observed in such an incompatible material, as characterized by differential scanning calorimetry (DSC) in Figure S1A (Supporting Information). Under the stress-free condition, we conducted a total of 573 thermal cycles for the $\text{CuAl}_{24}\text{Mn}_9$ alloy. After the thermal cycling, about $50 \text{ }^\circ\text{C}$ thermal hysteresis is accumulated, corresponding to more than $20 \text{ }^\circ\text{C}$ migration of transformation temperature. The same piece of $\text{CuAl}_{24}\text{Mn}_9$ alloy was taken for surface morphology observation under optical microscopy, as seen in Figure S1B (Supporting Information) after the 10th, 100th, 300th, and 500th cycles. The microstructure of the triple junction at the grain boundaries exhibits a clear trace of nonrecoverable deformations and cracking.

Under both optical microscope and scanning electron microscope (SEM), we identified a grain boundary across which the neighboring grains show sufficient contrast. By focused-ion beam (FIB) milling, several cylindrical pillars of $4 \text{ }\mu\text{m}$ diameter were fabricated in the neighboring grains and at the grain boundary in Figure 1a. The inset SEM images show the

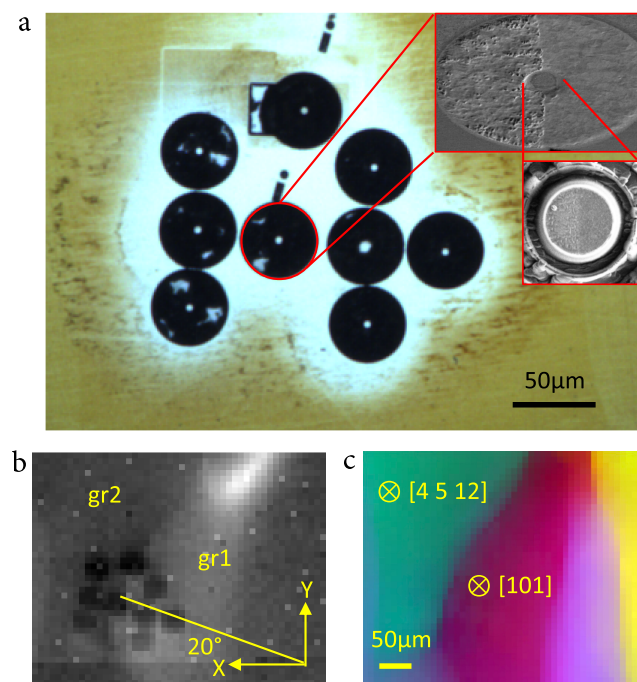


Figure 1. Morphology of grain boundary and the corresponding micropillar in austenite phase. (a) Optical micrograph of $\text{CuAl}_{24}\text{Mn}_9$ grain boundary structure with the inset of SEM image for the morphology of the bicrystal pillar at GB ab initio FIB milling. (b) Intensity map of the surface by scanning white-beam synchrotron X-ray. (c) Orientation map of the surface normal by synchrotron Laue microdiffraction.

trace of a grain boundary in a pillar. It indicates that the pillar is a bicrystal comprised of two different orientations. In order to quantitatively map the orientations of the neighboring grains and the GB, we conducted synchrotron X-ray Laue microdiffraction scan over several austenite grains, as in Figure 1b,c. By the intensity map obtained by averaging the pixelated intensity of each of the Laue patterns, we located the grain boundary and obtained its geometric normal as $\mathbf{g}\mathbf{b} = \cos \theta \mathbf{X} + \sin$

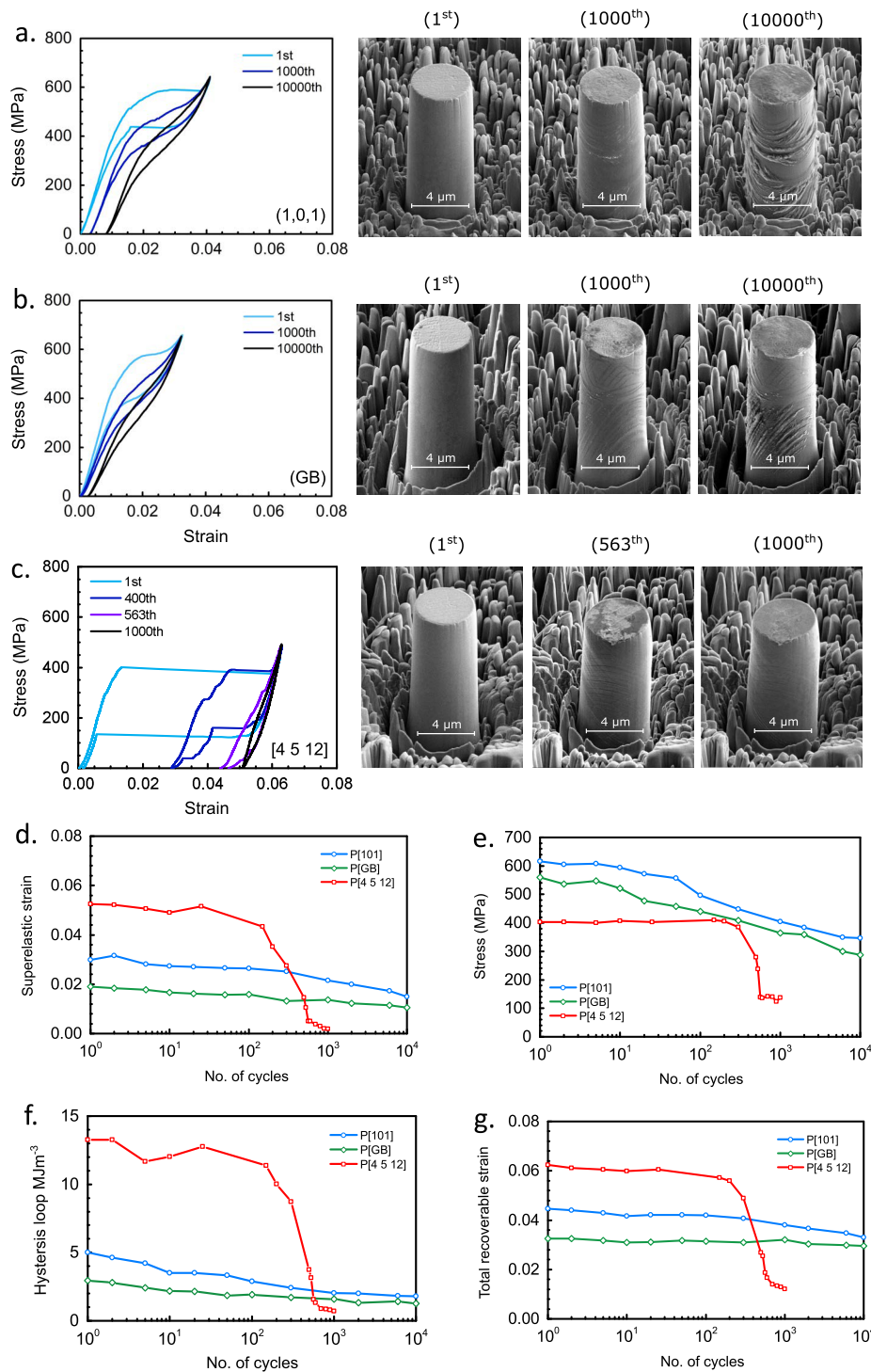


Figure 2. Nanomechanical behaviors and post-mortem images of $\text{CuAl}_{24}\text{Mn}_9$ $4\ \mu\text{m}$ -diameter pillars under cycling microcompression tests. (a) The single crystal pillar oriented along $[101]_{\text{gr}1}$. (b) The bicrystal pillar at the GB. (c) The single crystal pillar oriented along $[4\ 5\ 12]_{\text{gr}2}$. Their superelastic behaviors and the dissipation behaviors over stress-induced transformation cycles for $\text{CuAl}_{24}\text{Mn}_9$ $[101]_{\text{gr}1}$, GB, and $[4\ 5\ 12]_{\text{gr}2}$ pillars. Particularly, they are cyclic degradation of (d) superelastic strain. (e) Critical stress inducing phase transformation. (f) Area of hysteresis loop. (g) Recoverable strains.

θY relative to the sample basis X (rolling) – Y (transverse) – Z (normal). The GB normal angle $\theta = 20^\circ$ as seen from Figure 1b. Here we assume GB's Z component vanishes because we observed a cliff along the trace of GB, which is almost aligned with the longitudinal direction of the pillar during the FIB milling process. The neighboring grains are labeled as gr1 and gr2 in Figure 1b, whose orientations are characterized in Figure 1c. The sample axes are written in gr1 basis as

$$\begin{aligned} X &= [X]_{\text{gr}1} = [0.398, 0.160, -0.398]_{\text{gr}1} \approx [52\bar{5}]_{\text{gr}1} \\ Y &= [Y]_{\text{gr}1} = [-0.116, 0.563, 0.109]_{\text{gr}1} \approx [\bar{1}51]_{\text{gr}1} \\ Z &= [Z]_{\text{gr}1} = [0.414, 0.005, 0.414]_{\text{gr}1} \approx [101]_{\text{gr}1} \end{aligned} \quad (2)$$

Note that Z -direction is the end-surface direction of pillars along the compressive direction under nanoindentation. The end-

Table 2. Maximum Compressive Axial Strains for Single Crystal Pillars in $[101]_{\text{gr1}}$ and $[4\ 5\ 12]_{\text{gr2}}$

orientation	pair of variants	habit plane	shear vector	axial strain	Schmid factor $m_{(ij)}$
$[101]_{\text{gr1}}$	(3, 6)	$(-0.7535, -0.6327, 0.1787)_{\text{gr1}}$	$[0.0735, -0.0709, 0.0259]_{\text{gr1}}$	-0.02805	0.2712
	(3, 6)	$(-0.2556, -0.7072, -0.6592)_{\text{gr1}}$	$[-0.0174, -0.0626, 0.0829]_{\text{gr1}}$	-0.02805	0.2845
	(4, 5)	$(-0.6592, -0.7072, -0.2556)_{\text{gr1}}$	$[0.0829, -0.0626, -0.01738]_{\text{gr1}}$	-0.02805	0.2845
	(4, 5)	$(0.1787, -0.6327, -0.7535)_{\text{gr1}}$	$[0.02590, -0.07088, 0.07353]_{\text{gr1}}$	-0.02805	0.2712
$[4\ 5\ 12]_{\text{gr2}}$	(2, 5)	$(0.6321, -0.2549, -0.7318)_{\text{gr2}}$	$[0.0705, -0.0122, 0.0733]_{\text{gr2}}$	-0.04414	0.4371

surface normal of grain gr2 is written as $\mathbf{Z} = [\mathbf{Z}]_{\text{gr2}} \approx [4\ 5\ 12]_{\text{gr2}}$, which differs from $[\mathbf{Z}]_{\text{gr1}}$ by 33.73° . The orientations of grains gr1 and gr2 are related by a misorientation matrix \mathbf{Q} determined in Supporting Information.

The nanocompression cycling tests were conducted at a fixed loading rate of $200\ \mu\text{N/s}$ at room temperature by Hysitron TI 980 TriboIndenter. In each of the stress-induced transformation cycles, the pillar was loaded until the phase transformation from austenite to martensite completes, then fully unloaded to recover the superelastic deformation. The details are included in Materials and Methods in Supporting Information.

Figure 2a–c shows the stress–strain curves of pillars at various numbers of cycles from grain gr1, grain boundary, and grain gr2. The superelasticity is captured in all three micropillars, but their functionalities and corresponding degradations vary drastically. For single crystal pillar in $[101]_{\text{gr1}}$ grain and bicrystal pillar at GB in Figure 2a,b, the stress for inducing phase transformation is about 600 MPa, which is much higher than that for the single crystal pillar in $[4\ 5\ 12]_{\text{gr2}}$ grain in Figure 2c. In fact, this critical stress is one of the highest reported driving stresses in Cu-based shape memory alloys.^{4,18,26–28,33,34} Among the ternary CuAlMn alloys, the usual value of critical stress is below 300 MPa,^{26,27,34} and their superelasticity behaviors exhibit large degradations in the first few tens of cycles. In CuAl₂Mn₉ case, it is spectacular to see the stability of superelastic strain over 10 000 demanding mechanical cycles for the micropillars in $[101]_{\text{gr1}}$ grain and at the GB. For the single crystal micropillar in $[4\ 5\ 12]_{\text{gr2}}$ grain, significant degradation occurs after 600 cycles under much lower driving stress. From the post-mortem images of these pillars at the first and the last cycles, we can clearly see the longitudinal shortening in $[4\ 5\ 12]_{\text{gr2}}$ pillar but not in the other two pillars even under a higher number of mechanical cycles. In contrast to the thermal fatigue behavior of this alloy, the functional fatigue under stress-induced transformations in micropillars is much reduced for the special orientation. Note that the pillar size in our experiment is small but not sufficiently small to trigger a size effect of sudden strengthening.³⁵

Quantitative mechanics analysis over microcompressive cycles reveals that the bicrystal pillar at GB exhibits the lowest degradation for all functionalities plotted in Figure 2d–g. We use the plateau strain to represent the superelastic strain and use the onset stress of the plateau to represent the critical stress for inducing phase transformation. As in Figure 2d,e, the single crystal micropillar in $[4\ 5\ 12]_{\text{gr2}}$ grain delivers a large superelastic strain (i.e., 0.048) under stress of 400 MPa in its first few cycles, but the value sharply drops to near zero after 600 cycles. The single crystal micropillar in $[101]_{\text{gr1}}$ grain exhibits 0.029 superelastic strain under the stress of 610 MPa in the first cycle. Both superelastic strain and the driving stress gradually degrade to half of their original values after 10 000 cycles. The bicrystal pillar at GB shows 0.02 superelastic strain under the stress of 580 MPa in the first cycle, which sustains for 10 000 cycles with very subtle degradation. The energy dissipation is

represented by the area of the hysteresis loop upon loading and unloading, and the recoverability was expressed by the recoverable strain per cycle. The cyclic behaviors of these two functionalities were plotted in Figure 2f,g, with similar trends seen among the tested micropillars. Conventionally, a non-transforming GB would make the mechanical properties of polycrystalline solids worse upon large deformations, especially in Cu-based shape memory alloys.^{25,26} At a high-angle GB (about 34° angular misorientation), the mechanism that confines the recoverable strain and enhances the reversibility of the bicrystal pillar is unclear according to our nanomechanics experiments.

For a cubic to orthorhombic transformation, there exist six distinct martensite variants expressed by the symmetry-related stretch tensors in the set $\mathcal{M} = \{\mathbf{U}_1, \dots, \mathbf{U}_6\} = \{\bar{\mathbf{Q}}_i \mathbf{U} \bar{\mathbf{Q}}_i^T: \bar{\mathbf{Q}}_i \in \mathcal{P}^{24}/\mathcal{P}^4\}$ where \mathbf{U} is given in eq 1, the symbols \mathcal{P}^{24} and \mathcal{P}^4 denote the point group of cubic and orthorhombic lattices, respectively.^{12,22} The matrix forms and corresponding labels of these variants are given in Supporting Information. By symmetry, any pair of distinct variants $(\mathbf{U}_i, \mathbf{U}_j) \subset \mathcal{M}$ can form a twin as $\mathbf{R}\mathbf{U}_j = \mathbf{U}_i + \mathbf{a}_{(ij)} \otimes \mathbf{n}_{(ij)}$ for twinning plane normal $\mathbf{n}_{(ij)} \in \mathbb{R}^3$ and twinning shear $\mathbf{a}_{(ij)} \in \mathbb{R}^3$ subjected to some rotation $\mathbf{R} \in \text{SO}(3)$. (The symbol $\text{SO}(3)$ denotes the group of 3×3 orthogonal matrices with determinant 1.) In Supporting Information, we examined the twin relation for all pairwise variants summarized in the twin Table S1. Restricted by the crystallographic compatibility²²

$$\hat{\mathbf{R}}[(1-f)\mathbf{U}_i + f\mathbf{R}\mathbf{U}_j] - \mathbf{I} = \mathbf{b}_{(ij)} \otimes \mathbf{m}_{(ij)} \quad (3)$$

for some orthogonal matrix $\hat{\mathbf{R}} \in \text{SO}(3)$, vectors $\mathbf{b}_{(ij)}, \mathbf{m}_{(ij)} \in \mathbb{R}^3$ and the volume fraction $f \in [0, 1]$. All 12 pairs of variants can form 96 compatible twin laminates with austenite through a habit plane $\mathbf{m}_{(ij)}$ by a shear vector $\mathbf{b}_{(ij)}$. Here, we use $\mathbf{F}_{(ij)} = \mathbf{I} + \mathbf{b}_{(ij)} \otimes \mathbf{m}_{(ij)}$ to express the averaged deformation gradient of the compatible twin laminates (i, j) that solve eq 3. Supposing that the pillar completely transforms from austenite to twinned martensite, the averaged axial strain of the pillar under uniaxial loading is defined as

$$\epsilon_{(ij)} = \sqrt{\mathbf{c} \cdot \mathbf{F}_{(ij)}^T \mathbf{F}_{(ij)} \mathbf{c}} - 1 \quad (4)$$

where $\mathbf{c} \in \mathbb{R}^3$ is a unimodular vector along the loading axis. In our nanocompression experiment, it is required that $\epsilon_{(ij)} < 0$. According to energy minimization,^{12,22,36} the pair of martensite variants that would appear upon the uniaxial compressive stress-induced phase transformation should be the maximizer of the strain function along compressing direction, that is

$$(i^*, j^*) = \arg \max_{\epsilon_{(ij)} < 0} |\epsilon_{(ij)}| \quad (5)$$

For single crystal micropillars, the axial loading direction is aligned with $[101]_{\text{gr1}}$ for grain gr1 and $[4\ 5\ 12]_{\text{gr2}}$ for grain gr2.

We calculated the maximum compressive strains for each of the orientations among all compatible twin laminates, summarized in Table 2. For the single crystal micropillar in grain gr1, two crystallographically equivalent pairs of variants (U_3, U_6) and (U_4, U_5) offer the same superelastic strain, $\epsilon_{(3,6)} = \epsilon_{(4,5)} = -0.02805$ that agree with the superelastic plateau strain in the nanomechanics experiment (Figure 2a). For the single crystal micropillar in grain gr2, there is only one pair of variants (U_2, U_5) corresponding to -0.04414 superelastic strain, which also matches the superelastic plateau strain in experiment. However, the measured superelastic strain of bicrystal pillar at GB does not agree with the linear mixtures of the axial strains contributed by the orientations $[101]_{gr1}$ and $[4\ 5\ 12]_{gr2}$.

Beyond the energetic constraint on axial compression, the compatible twin laminates tend to minimize the lateral shear deformation.¹⁸ Among the crystallographically compatible twin laminates, the resolved shear, that is, Schmid factor for twinning³⁷ along the austenite/martensite interface, should be minimized. For the unimodular vector \mathbf{c} along the loading direction, the twinning Schmid factor is defined as

$$m_{(i,j)} = \frac{|\mathbf{c} \cdot \mathbf{m}_{(i,j)}| |\mathbf{c} \cdot \mathbf{b}_{(i,j)}|}{|\mathbf{m}_{(i,j)}| |\mathbf{b}_{(i,j)}|} \quad (6)$$

For the single crystal oriented in $[101]_{gr1}$, the minimum twinning Schmid factor is 0.2712, corresponding to the habit planes

$$\mathbf{m}_{(3,6)} = (-0.7535, -0.6327, 0.1787)_{gr1}$$

and

$$\mathbf{m}_{(4,5)} = (0.1787, -0.6327, -0.7535)_{gr1}$$

For the single crystal oriented in $[4\ 5\ 12]_{gr2}$, the twinning Schmid factor is 0.4371 that almost reaches the maximum possible Schmid factor for an fcc crystal. These results imply that the slip by dislocations along $\mathbf{m}_{(2,5)}$ in $[4\ 5\ 12]_{gr2}$ pillar is much easier than that in $[101]_{gr1}$ pillar, therefore the accumulated residual plastic deformations are much larger in grain gr2 over mechanical-induced transformation cycles.

The normal of grain boundary written in grain gr1 basis is $\mathbf{g}\mathbf{b} = [0.574, 0.585, -0.574]_{gr1}$, almost parallel to $[11\bar{1}]_{gr1}$. If we use the twin laminates as the building blocks to derive the microstructure for the bicrystal pillar at GB, as shown in Figure 3a,b, the deformed configurations of either (3,6) or (4,5) twin laminates in grain gr1 are subjected to a very large discontinuity from the (2,5) twin laminates in grain gr2 at the grain boundary. To mediate such a spatial cracking at the GB, the pairs of variants in neighboring grains need to minimize both the areal and directional differences of the GB deformed from two sides. For two orthonormal vectors \mathbf{r}_1 and \mathbf{r}_2 such that $\mathbf{r}_1 \cdot \mathbf{g}\mathbf{b} = \mathbf{r}_2 \cdot \mathbf{g}\mathbf{b} = 0$, the pairs of twin variants in neighboring grains should satisfy

$$(i^*, j^*, k^*, l^*) = \arg \min_{(i,j),(k,l) \in C} D_{(i,j,k,l)} \quad (7)$$

where C denotes the set of all pairs of variants of $\text{CuAl}_{24}\text{Mn}_9$ that solve the crystallographic eq 3. The function $D_{(i,j,k,l)}$ is defined as the GB-compatibility metric

$$D_{(i,j,k,l)} = |\text{cof}(\mathbf{b}_{(i,j)} \otimes \mathbf{m}_{(i,j)} - \tilde{\mathbf{b}}_{(k,l)} \otimes \tilde{\mathbf{m}}_{(k,l)}) \mathbf{g}\mathbf{b}| + \sum_{s=1,2} |(\mathbf{m}_{(i,j)} \cdot \mathbf{r}_s) \mathbf{b}_{(i,j)} - (\tilde{\mathbf{m}}_{(k,l)} \cdot \mathbf{r}_s) \tilde{\mathbf{b}}_{(k,l)}| \quad (8)$$

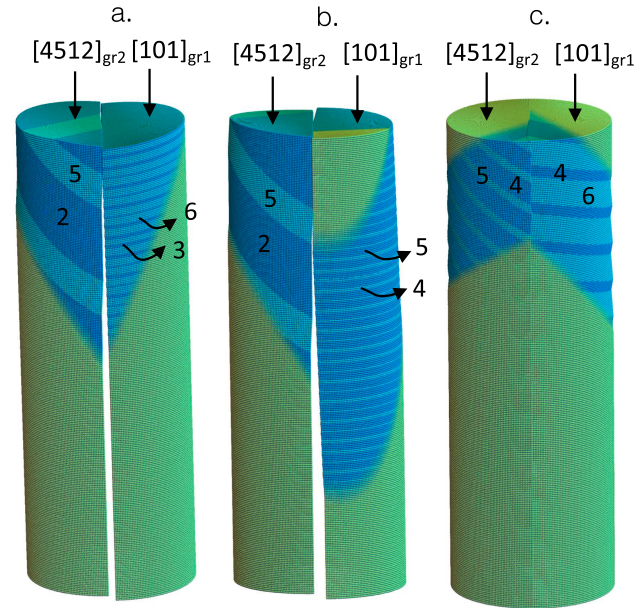


Figure 3. Theoretical calculation of twinning microstructure in the bicrystal pillar at GB for (a) (3,6) variants of grain gr1 and (2,5) variants of grain gr2, (b) (4,5) variants of grain gr1 and (2,5) variants of grain gr2 and (c) (4,6) variants of grain gr1 and (4,5) variants of grain gr2. The light green color refers to the domain of austenite phase.

where $\tilde{\mathbf{b}}_{(k,l)} = \mathbf{Q}\mathbf{b}_{(k,l)}$, and $\tilde{\mathbf{m}}_{(k,l)} = \mathbf{Q}\mathbf{m}_{(k,l)}$ for the misorientation matrix \mathbf{Q} characterized by synchrotron Laue microdiffraction. In eq 8, the first term calculates the areal jump, and the second term calculates the sum of the directional differences from one side of GB to the other.

We examined all compatible twin laminates and identified the type II twin formed by a pair of variants (4,6) in grain gr1 and the type I twin formed by pair of variants (4,5) in grain gr2 are the minimizers of eq 7. The GB-compatibility metric of (4,6) and (4,5) laminates is calculated as $D_{(4,6,4,5)} = 0.000407$. Note that the GB-compatibility metric is an area measure, while the crystallographic compatibility metric λ_2 is an axial length measure along the middle eigenvector of the transformation stretch tensor. In this material, the square of the crystallographic compatibility, $|\lambda_2 - 1|^2 = 0.00065$ is comparable to the GB-compatibility metric. It implies that two-tier compatibility coexists in this polycrystalline alloy to make it highly reversible. The deformed configuration of these GB-compatible twin laminates are drawn in Figure 3c, which fit together nicely from opposite sides. The GB-compatibility metric given by eq 8 offers a new kinematic constraint on microstructure formation, which guarantees the spatial continuity at the high-angle grain boundary. In other words, the crystallographically compatible twins accommodate themselves to mediate the discontinuity at GB.

Moreover, the GB-compatible twin laminates (4,6) and (4,5) act as the interlock that prevents the shear deformation crossing over the grain boundary. The habit planes and corresponding shear vectors are expressed as

$$[101]_{gr1}: \mathbf{m}_{(4,6)} = (-0.7318, -0.6321, -0.2549)_{gr1}$$

$$\mathbf{b}_{(4,6)} = (0.0733, -0.0705, -0.0122)_{gr1}$$

with twinning Schmid factor $m_{(4,6)} = 0.29403$, and

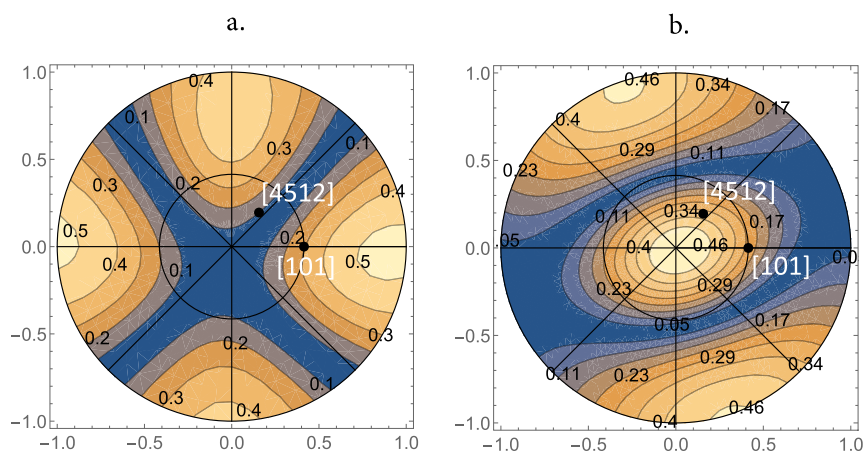


Figure 4. Contours of the Schmid factors for the twin laminates of (a) type II twin (4,6) variants in $[101]_{gr1}$ orientation and (b) type I twin (4,5) variants in $[4\ 5\ 12]_{gr2}$ orientation.

$$[4512]_{gr2}: \mathbf{m}_{(4,5)} = (0.1787, -0.6327, -0.7535)_{gr2}$$

$$\mathbf{b}_{(4,5)} = (0.0255, -0.0709, 0.0735)_{gr2}$$

with twinning Schmid factor $m_{(4,5)} = 0.37445$. Compared to $m_{(2,5)} = 0.4371$ in single crystal micropillar in axial direction $[4\ 5\ 12]_{gr2}$, the twinning Schmid factor of the bicrystal micropillar in grain $[4\ 5\ 12]_{gr2}$ is very reduced and is associated with a low risk of plastic deformations.

Figure 4a,b shows the orientation-dependent twinning Schmid factors for the type II twin (4,6) and type I twin (4,5) respectively. In the bicrystal micropillar, the twin (4,6) has a higher twinning Schmid factor in the grain gr1, while the twin (4,5) has a higher twinning Schmid factor in the grain gr2. When gliding dislocations travel from one grain to the other through the GB, a sudden decrease of the Schmid factor will prevent them from proceeding. As a consequence, the dislocations are trapped at the GB and the accumulation of plastic deformations over cycles could be much lessened. The axial strains given by the GB-compatible twin laminates are both lower than the values given by the twins developed in the single crystal micropillars. It provides a reasonable explanation for the reduced plateau strain in Figure 2c under stress-induced phase transformation.

To summarize, this paper combines the crystallographic compatibility and grain boundary morphology to derive a two-tier compatibility mechanism for polycrystalline shape memory alloys. Through a rational measurement of the cyclic superelastic behaviors in a phase-transforming bicrystal micropillar, we showed that both the crystallography and kinematics properties of GB play an important role in formation of microstructure in adjacent grains. For specific neighboring textures, the GB-compatibility ensures that the twins near the boundary minimize the spatial crack and act as an interlock to prevent dislocations from slipping from one grain to the other, thus enhancing the reversibility of the transforming metals over mechanical cycles. This work provides an important insight for the development of superelastic microdevices and may foster the applications of Cu-based SMAs for precise microstents and other biomedical applications.

■ ASSOCIATED CONTENT

SI Supporting Information

The Supporting Information is available free of charge at <https://pubs.acs.org/doi/10.1021/acs.nanolett.0c03486>.

Supplementary text, Figures S1 and S2, Table S1, additional references (PDF)

■ AUTHOR INFORMATION

Corresponding Author

Xian Chen – Department of Mechanical and Aerospace Engineering, Hong Kong University of Science and Technology, Hong Kong; orcid.org/0000-0002-0114-4642; Email: xianchen@ust.hk

Authors

Mostafa Karami – Department of Mechanical and Aerospace Engineering, Hong Kong University of Science and Technology, Hong Kong

Zeyuan Zhu – Department of Mechanical and Aerospace Engineering, Hong Kong University of Science and Technology, Hong Kong

Zhuohui Zeng – Department of Mechanical and Aerospace Engineering, Hong Kong University of Science and Technology, Hong Kong

Nobumichi Tamura – Advanced Light Source, Lawrence Berkeley National Lab, Berkeley, California 94720, United States

Yong Yang – Mechanical Engineering, City University of Hong Kong, Kowloon, Hong Kong

Complete contact information is available at:

<https://pubs.acs.org/10.1021/acs.nanolett.0c03486>

Notes

The authors declare no competing financial interest.

■ ACKNOWLEDGMENTS

M.K., Z. Zhu, Z. Zeng, and X.C. thank the HK Research Grants Council for financial support under Grants 16207017 and 16201019. Beamline 12.3.2 and the Advanced Light Source were supported by the Office of Science, Office of Basic Energy Sciences, of the U.S. Department of Energy under Contract No. DE-AC02-05CH11231.

■ REFERENCES

- (1) Busch, J. D.; Johnson, A. D. Shape-memory alloy micro-actuator. 1991; U.S. Patent 5,061,914.
- (2) Kahn, H.; Huff, M. A.; Heuer, A. H. The TiNi shape-memory alloy and its applications for MEMS. *J. Micromech. Microeng.* **1998**, *8*, 213–221.

- (3) Yoneyama, T.; Miyazaki, S. *Shape memory alloys for biomedical applications*; CRC Press: Boca Raton, FL, 2008.
- (4) Juan, J. S.; No, M. L.; Schuh, C. A. Nanoscale shape-memory alloys for ultrahigh mechanical damping. *Nat. Nanotechnol.* **2009**, *4*, 415–419.
- (5) AbuZaiter, A.; Nafea, M.; Mohamed Ali, M. S. Development of a shape-memory-alloy micromanipulator based on integrated bimorph microactuators. *Mechatronics* **2016**, *38*, 16–28.
- (6) Gómez-Cortés, J. F.; NÓ, M. L.; Ruíz-Larrea, I.; Breczewski, T.; López-Echarri, A.; Schuh, C. A.; San Juan, J. M. Ultrahigh superelastic damping at the nano-scale: A robust phenomenon to improve smart MEMS devices. *Acta Mater.* **2019**, *166*, 346–356.
- (7) Bechtold, C.; Lima de Miranda, R.; Chluba, C.; Zamponi, C.; Quandt, E. Method for fabricating miniaturized NiTi self-expandable thin film devices with increased radiopacity. *Shap. Mem. Superelasticity* **2016**, *2*, 391–398.
- (8) Wohlschlägel, M.; Lima de Miranda, R.; Schüssler, A.; Quandt, E. Nitinol: Tubing versus sputtered film—microcleanliness and corrosion behavior. *J. Biomed. Mater. Res., Part B* **2016**, *104*, 1176–1181.
- (9) Auricchio, F.; Boatti, E.; Conti, M. In *Shape Memory Alloy Engineering*; Concilio, A., Lecce, L., Eds.; Elsevier, 2015; Chapter 11, pp 307–341.
- (10) Chen, Y.; Howe, C.; Lee, Y.; Cheon, S.; Yeo, W.-H.; Chun, Y. Microstructured thin film nitinol for a neurovascular flow-diverter. *Sci. Rep.* **2016**, *6*, 23698.
- (11) Chen, X.; Srivastava, V.; Dabade, V.; James, R. D. Study of the cofactor conditions: conditions of supercompatibility between phases. *J. Mech. Phys. Solids* **2013**, *61*, 2566–2587.
- (12) Ball, J.; James, R. Fine phase mixtures as minimizers of energy. *Arch. Ration. Mech. Anal.* **1987**, *100*, 13–52.
- (13) Chen, X.; Song, Y.; Tamura, N.; James, R. D. Determination of the stretch tensor for structural transformations. *J. Mech. Phys. Solids* **2016**, *93*, 34–43.
- (14) Cui, J.; Chu, Y. S.; Famodu, O. O.; Furuya, Y.; Hatrick-Simpers, J.; James, R. D.; Ludwig, A.; Thienhaus, S.; Wuttig, M.; Zhang, Z.; et al. Combinatorial search of thermoelastic shape-memory alloys with extremely small hysteresis width. *Nat. Mater.* **2006**, *5*, 286–290.
- (15) Zhang, Z.; James, R. D.; Müller, S. Energy barriers and hysteresis in martensitic phase transformations. *Acta Mater.* **2009**, *57*, 4332–4352.
- (16) Song, Y.; Chen, X.; Dabade, V.; Shield, T. W.; James, R. D. Enhanced reversibility and unusual microstructure of a phase-transforming material. *Nature* **2013**, *502*, 85–88.
- (17) Chluba, C.; Ge, W.; Lima de Miranda, R.; Strobel, J.; Kienle, L.; Quandt, E.; Wuttig, M. Ultralow-fatigue shape memory alloy films. *Science* **2015**, *348*, 1004–1007.
- (18) Ni, X.; Greer, J. R.; Bhattacharya, K.; James, R. D.; Chen, X. Exceptional resilience of small-scale $\text{Au}_{30}\text{Cu}_{25}\text{Zn}_{45}$ under cyclic stress-induced phase transformation. *Nano Lett.* **2016**, *16*, 7621–7625.
- (19) Jetter, J.; Gu, H.; Zhang, H.; Wuttig, M.; Chen, X.; Greer, J. R.; James, R. D.; Quandt, E. Tuning crystallographic compatibility to enhance shape memory in ceramics. *Phys. Rev. Mater.* **2019**, *3*, No. 093603.
- (20) Pang, E. L.; McCandler, C. A.; Schuh, C. A. Reduced cracking in polycrystalline $\text{ZrO}_2\text{-CeO}_2$ shape-memory ceramics by meeting the cofactor conditions. *Acta Mater.* **2019**, *177*, 230–239.
- (21) Yin, H.; He, Y.; Moumni, Z.; Sun, Q. Effects of grain size on tensile fatigue life of nanostructured NiTi shape memory alloy. *Int. J. Fatigue* **2016**, *88*, 166–177.
- (22) Bhattacharya, K. In *Microstructure of martensite: why it forms and how it gives rise to the shape-memory effect*; Sutton, A. P., Rudd, R. E., Eds.; Oxford University Press, 2003; Vol. 2.
- (23) Kabirifar, P.; Chu, K.; Ren, F.; Sun, Q. Effects of grain size on compressive behavior of NiTi polycrystalline superelastic macro- and micropillars. *Mater. Lett.* **2018**, *214*, 53–55.
- (24) Hua, P.; Chu, K.; Ren, F.; Sun, Q. Cyclic phase transformation behavior of nanocrystalline NiTi at microscale. *Acta Mater.* **2020**, *185*, 507–517.
- (25) Funakubo, H.; Kennedy, J. *Shape memory alloys*; Gordon and Breach, 1987; xii–275.
- (26) Zárubová, N.; Novák, V. Phase stability of CuAlMn shape memory alloy. *Mater. Sci. Eng., A* **2004**, *378*, 216–221.
- (27) Sutou, Y.; Omori, T.; Kainuma, R.; Ishida, K.; Ono, N. Enhancement of superelasticity in Cu-Al-Mn-Ni shape-memory alloys by texture control. *Metall. Mater. Trans. A* **2002**, *33*, 2817–2824.
- (28) Fornell, J.; Tuncer, N.; Schuh, C. Orientation dependence in superelastic Cu-Al-Mn-Ni micropillars. *J. Alloys Compd.* **2017**, *693*, 1205–1213.
- (29) Karami, M.; Tamura, N.; Yang, Y.; Chen, X. Derived crystal structure of martensitic materials by solid–solid phase transformation. *Acta Crystallogr., Sect. A: Found. Adv.* **2020**, *76*, 521–533.
- (30) Chen, X.; Dejoie, C.; Jiang, T.; Ku, C.-S.; Tamura, N. Quantitative microstructural imaging by scanning Laue x-ray micro- and nanodiffraction. *MRS Bull.* **2016**, *41*, 445–453.
- (31) Otsuka, K.; Ohba, T.; Tokonami, M.; Wayman, C.M. New description of long period stacking order structures of martensites in β -phase alloys. *Scr. Metall. Mater.* **1993**, *29*, 1359–1364.
- (32) Chakravorty, S.; Wayman, C. Electron microscopy of internally faulted Cu-Zn-Al martensite. *Acta Metall.* **1977**, *25*, 989–1000.
- (33) Liu, J.-L.; Huang, H.-Y.; Xie, J.-X. The roles of grain orientation and grain boundary characteristics in the enhanced superelasticity of $\text{Cu}_{71.8}\text{Al}_{17.8}\text{Mn}_{10.4}$ shape memory alloys. *Mater. Eng.* **2014**, *64*, 427–433.
- (34) Dutkiewicz, J.; Kato, H.; Miura, S.; Messerschmidt, U.; Bartsch, M. Structure changes during pseudoelastic deformation of CuAlMn single crystals. *Acta Mater.* **1996**, *44*, 4597–4609.
- (35) Gómez-Cortés, J. F.; NÓ, M. L.; López-Ferreño, I. n.; Hernández-Saz, J.; Molina, S. I.; Chuvilin, A.; San Juan, J. M. Size effect and scaling power-law for superelasticity in shape-memory alloys at the nanoscale. *Nat. Nanotechnol.* **2017**, *12*, 790–797.
- (36) Bhattacharya, K.; Kohn, R. V. Symmetry, texture and the recoverable strain of shape-memory polycrystals. *Acta Mater.* **1996**, *44*, 529–542.
- (37) Shu, Y.; Bhattacharya, K. The influence of texture on the shape-memory effect in polycrystals. *Acta Mater.* **1998**, *46*, 5457–5473.